Photochemical & Photobiological Sciences (2023) 22:2093–2104
https://doi.org/10.1007/s43630-023-00432-2

ORIGINAL PAPERS

Concerning the photophysics of fluorophores towards tailored bioimaging compounds: a case study involving S100A9 inflammation markers

Simon T. Steiner[1] · Iván Maisuls[2,3] · Anna Junker[1] · Günter Fritz[4] · Andreas Faust[1] · Cristian A. Strassert[2,3]

Received: 5 December 2022 / Accepted: 28 April 2023 / Published online: 11 June 2023

Abstract

A full understanding concerning the photophysical properties of a fluorescent label is crucial for a reliable and predictable performance in biolabelling applications. This holds true not only for the choice of a fluorophore in general, but also for the correct interpretation of data, considering the complexity of biological environments. In the frame of a case study involving inflammation imaging, we report the photophysical characterization of four fluorescent S100A9-targeting compounds in terms of UV–vis absorption and photoluminescence spectroscopy, fluorescence quantum yields (Φ_F) and excited state lifetimes (τ) as well as the evaluation of the radiative and non-radiative rate constants (k_r and k_{nr}, respectively). The probes were synthesized based on a 2-amino benzimidazole-based lead structure in combination with commercially available dyes, covering a broad color range from green (6-FAM) over orange (BODIPY-TMR) to red (BODIPY-TR) and near-infrared (Cy5.5) emission. The effect of conjugation with the targeting structure was addressed by comparison of the probes with their corresponding dye-azide precursors. Additionally, the 6-FAM and Cy5.5 probes were measured in the presence of murine S100A9 to determine whether protein binding influences their photophysical properties. An interesting rise in Φ_F upon binding of 6-FAM-SST177 to murine S100A9 enabled the determination of its dissociation equilibrium constant, reaching up to $K_D = 324$ nM. This result gives an outlook for potential applications of our compounds in S100A9 inflammation imaging and fluorescence assay developments. With respect to the other dyes, this study demonstrates how diverse microenvironmental factors can severely impair their performance while rendering them poor performers in biological media, showing that a preliminary photophysical screening is key to assess the suitability of a particular luminophore.

Keywords Fluorescent conjugates · S100A9 · Fluorescence quantum yields · Fluorescence lifetimes

1 Introduction

The alarmin heterocomplex S100A8/A9 is released during tissue damage and cellular stress and is hereby involved as an early amplifier in inflammatory processes [1]. Its local and massive excretion by phagocytes at the site of inflammation makes S100A8/A9 a suitable biomarker for inflammatory disorders associated with phagocyte activation, including autoimmune diseases, rheumatoid arthritis, allergies, cardiovascular diseases, Alzheimer's disease and tumors [2–6]. Therefore, S100A9-targeting compounds are the subject of research as therapeutic drugs or molecular imaging probes. Representative examples are quinoline-carboxamide inhibitors like Laquinimod and Tasquinimod, which were/are in clinical trials for the treatment of multiple sclerosis (Phase III), Huntington´s (Phase II) and Crohn´s diseases (Phase II) with Laquinimod, as well as different cancer types in the

✉ Cristian A. Strassert
ca.s@wwu.de

1 European Institute for Molecular Imaging, Westfälische Wilhelms-Universität Münster, Röntgenstraße 16, 48149 Münster, Germany

2 Institut für Anorganische und Analytische Chemie, CiMIC, SoN, Westfälische Wilhelms-Universität Münster, Corrensstraße 28/30, 48149 Münster, Germany

3 Center for Nanotechnology, Westfälische Wilhelms-Universität Münster, Heisenbergstraße 11, 48149 Münster, Germany

4 Cellular Microbiology, Institute of Biology, University of Hohenheim, Garbenstr. 30, 70599 Stuttgart, Germany

case of Tasquinimod [7–11]. In molecular imaging, a Cy5.5-labelled S100A9-specific antibody was successfully applied to visualize inflammation in various mouse models, such as irritant and allergic contact dermatitis, collagen-induced arthritis and *Leishmania major* infection [12]. The S100A9-targeting small-molecule probe Cy5.5-CES271 showed good optical signal accumulation in irritant contact dermatitis and LPS-induced lung inflammation mouse models [13, 14]. For both the development of therapeutic drugs and imaging agents, depending on the choice of the fluorophore, the fluorescent S100A9-binding probes open the way to various types of fluorescence-based (binding) assays and imaging applications.

A full understanding of the optical properties of a fluorescent compound is key for reliable and predictable performance in biological applications. This is especially true considering the complexity of biological systems: solvent effects and chemical surroundings, such as buffer constitution, pH value, ionic strength, viscosity and the presence of biomolecules or cell preparations, might affect not only binding but also the photophysical properties of a compound [15]. Furthermore, for an in vivo context, many additional factors such as pharmacokinetics, tissue penetration depth, plasma protein binding and cell permeation ability affect the optical signal [16]. The polarity and solubility of a dye is another point to consider, depending on the planned biological experiment: on the one hand, nonpolar dyes tend to show aggregation in an aqueous environment and a high degree of unspecific binding to lipophilic off-target structures while showing better cell permeation [17–19]. On the other hand, ionic and polar dyes are less prone to aggregation and unspecific binding, which leads to a strong optical signal and images with high signal-to-noise ratios, but with negligible cell permeation ability [15, 20]. All these parameters might have an influence on the absorption and emission spectra, but especially on the luminescence quantum yield (Φ_L) and luminescence lifetime (τ_L). Calculated from Φ_L and τ_L, the radiative and non-radiative decay rate constants k_r and k_{nr} (equations in S5) are key properties of a fluorophore, as changes in k_r and k_{nr} upon conjugation to a (targeting-) molecule or in different chemical surroundings can give insights into possible intra- and intermolecular interactions with the fluorophore [15] including physical or chemical quenching as well as aggregation phenomena.

In this study, we present the photophysical characterization of four fluorescent S100A9-targeting compounds in comparison with their corresponding dye-azide precursors in terms of UV–vis absorption and photoluminescence spectroscopy, fluorescence quantum yields (Φ_F) and lifetimes (τ_F). For our compounds, we chose a 2-amino benzimidazole-based lead structure that was reported as a S100A9 inhibitor with an efficient synthesis and superior inhibition compared to the quinoline-carboxamides [21, 22]. Based on this, we prepared four fluorescent compounds from commercially available organic dyes in a broad color range from green (6-FAM) over orange (BODIPY-TMR) to red (BODIPY-TR) and NIR (Cy5.5) emission. Our study showed the role of intra-molecular quenching of the 6-FAM-conjugate mediated by the targeting unit, as well as quenching of the lipophilic BODIPY-derivatives in aqueous solution due to aggregation and insolubility, whereas the highly ionic Cy5.5-labeled targeting compound matched the expected optical properties found in the literature. The effect of protein binding was investigated for the water-soluble 6-FAM- and Cy5.5-conjugates, which revealed a drop in Φ_F and k_r by a factor ~ 4 for Cy5.5-SST110 in the presence of murine S100A9. Therefore, Cy5.5-SST110 was not considered for further in vitro binding studies. Interestingly, the opposite effect was observed for the initially quenched 6-FAM-SST177 with a rise in Φ_F upon binding. This unique photophysical property enabled the determination of the dissociation equilibrium constant K_D of 6-FAM-SST177 towards murine S100A9 while giving an outlook on its application in future S100A9 binding studies.

2 Experimental section

2.1 General

Materials, methods, as well as synthetic procedures and analytical data, are provided in the supporting information.

2.2 Synthesis

Briefly, the lead targeting structure is built in a "3-step-one pot" synthesis (Scheme 1), starting from an amide, ethyl 3,3,3-trifluoropyruvate and 2-amino benzimidazole *via* an acyl-imin intermediate [21, 24]. The fluoro-pyridine moiety is substituted in a nucleophilic aromatic substitution with propargyl amine in a microwave reactor at 100 °C for 15 min, yielding the alkyne precursor [25]. The alkyne precursor was reacted in a copper mediated [3 + 2] dipolar cycloaddition with the corresponding dye-azide yielding the four target molecules.

2.3 Photophysical measurements

UV–vis absorption spectra were measured on a Shimadzu UV-3600 I plus UV–VIS-NIR spectrophotometer. Photoluminescence quantum yields were measured with a Hamamatsu Photonics absolute PL quantum yield measurement system (C9920-02) equipped with a L9799-01 CW Xe light source (150 W), a monochromator, a C7473 photonic multi-channel analyzer, an integrating sphere and employing

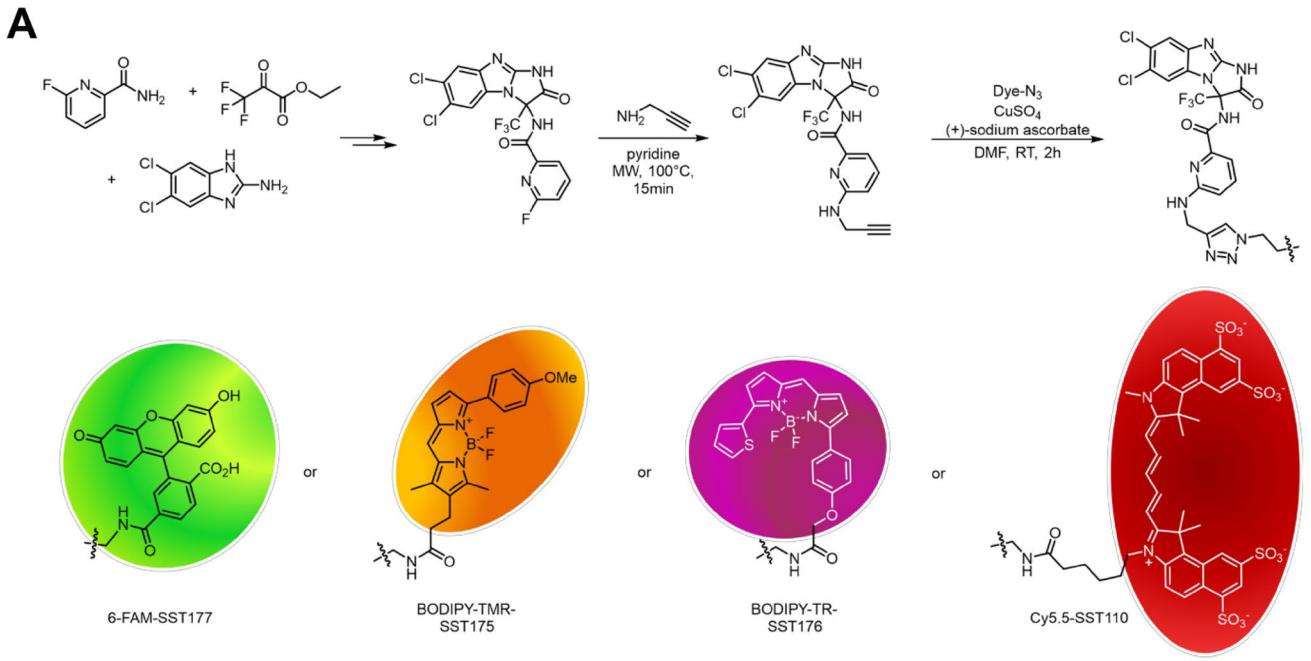

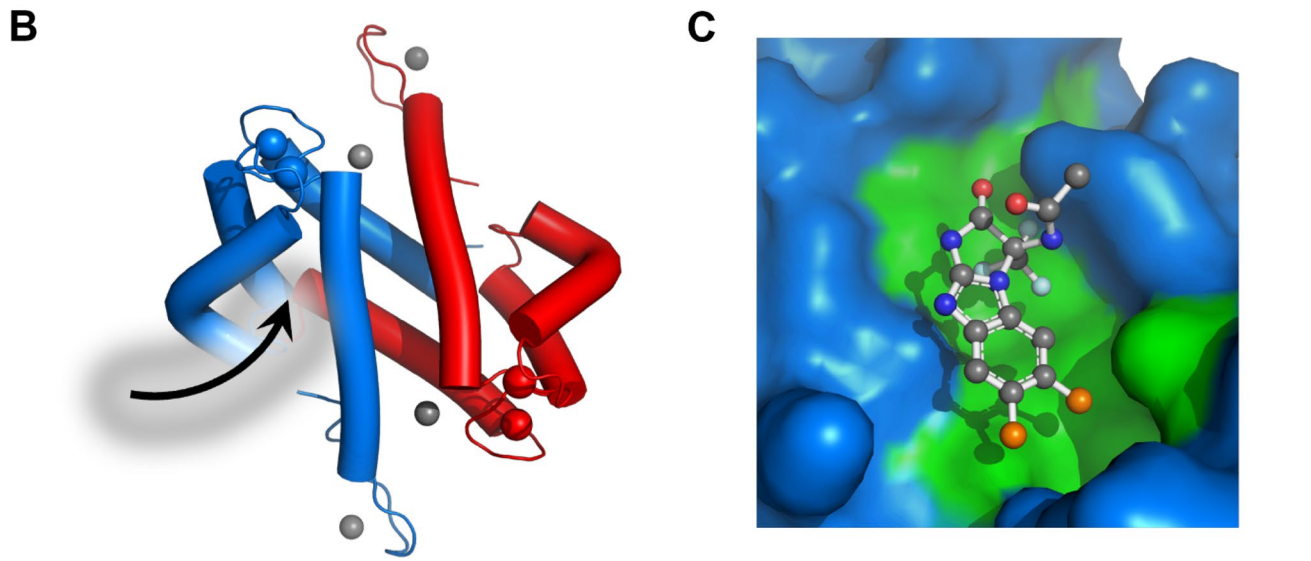

Scheme 1 **A** Synthesis of four fluorescent S100A9-targeting compounds based on the 2-amino benzimidazole lead structure and the commercially available dyes 6-FAM-azide, BODIPY-TMR-azide, BODIPY-TR-azide and Cy5.5-azide [21, 23]. **B** The structure of the murine S100A9 homodimer (pdb code 6ZFE) is depicted. The subunits are shown in red and blue. The bound Ca^{2+} (red/blue) and Zn^{2+} (grey) cations are highlighted as spheres. The arrow indicates the location of the compound binding site. **C** Close-up of the hydrophobic region of S100A9. The core of a 2-amino benzimidazole-based lead structure was modeled manually to the hydrophobic region highlighted in green. Carbon atoms are shown in grey, nitrogen in blue, oxygen in red, fluorine in light-blue, and chlorine in orange

U6039-05 software (Hamamatsu Photonics, Ltd., Shizuoka, Japan).

Steady-state excitation and emission spectra were recorded on a FluoTime 300 spectrometer from PicoQuant equipped with: a 300 W ozone-free Xe lamp (250–900 nm), a 10 W Xe flash-lamp (250–900 nm, pulse width *ca.* 1 µs) with repetition rates of 0.1–300 Hz, a double-grating excitation monocromator (Czerny-Turner type, grating with 1200 lines/mm, blaze wavelength: 300 nm), diode lasers (pulse width < 80 ps) operated by a computer-controlled laser driver PDL-828 "Sepia II" (repetition rate up to 80 MHz, burst mode for slow and weak decays), two double-grating emission monochromators (Czerny-Turner, selectable gratings blazed at 500 nm with 2.7 nm/mm

dispersion and 1200 lines/mm, or blazed at 1200 nm with 5.4 nm/mm dispersion and 600 lines/mm) with adjustable slit width between 25 µm and 7 mm, Glan–Thompson polarizers for excitation (after the Xe-lamps) and emission (after the sample). Different sample holders (Peltier-cooled mounting unit ranging from − 15 to 110 °C or an adjustable front-face sample holder), along with two detectors (namely a PMA Hybrid-07 from PicoQuant with transit time spread FWHM < 50 ps, 200–850 nm, or a H10330C-45-C3 NIR detector with transit time spread FWHM 0.4 ns, 950–1700 nm from Hamamatsu) were used. Steady-state spectra and photoluminescence lifetimes were recorded in TCSPC mode by a PicoHarp 300 (minimum base resolution 4 ps) or in MCS mode by a TimeHarp 260 (where up to several ms can be traced). Emission and excitation spectra were corrected for source intensity (lamp and grating) by standard correction curves. For samples with lifetimes in the ns order, an instrument response function calibration (IRF) was performed using a diluted Ludox® dispersion. Lifetime analysis was performed using the commercial EasyTau 2 software (PicoQuant). The quality of the fit was assessed by minimizing the reduced chi squared function (χ^2) and visual inspection of the weighted residuals and their autocorrelation. All solvents used were of spectrometric grade (Uvasol® from Merck).

2.4 Determination of K_D of 6-FAM-SST177 towards mS100A9

The experiments were performed in HPS buffer (50 mM HEPES, 1 mM $CaCl_2$, pH = 7.4), using black, flat-bottom 96-well plates (Thermo-Fisher, Waltham, USA, cat. no. 237108) and Flexstation 3 multi-mode microplate reader (Molecular devices, San José, USA). Murine S100A9 was diluted from a 110 µm stock solution in HPS (pH = 7.4), stored at − 20 °C in aliquots. 2 molar equivalents of $ZnCl_2$ were added to the protein solution and it was gently shaken at 37 °C for 30 min before experiments. 6-FAM-SST177 was diluted from a 10 mM DMSO stock solution and stored at − 30 °C under the exclusion of light. Samples with 6-FAM-SST177 (fixed concentration 25 nM) and increasing concentrations of murine S100A9 ranging from 40 nM to 10 µM in a volume of 100 µL per well were prepared as duplicates and incubated at 37 °C for 30 min prior to measurement. Fluorescence intensity was measured at $\lambda_{excitation} = 485$ nm and $\lambda_{detection} = 535$ nm with a 530 nm cut-off filter. The fluorescence intensity was blank-normalized (25 nm 6-FAM-SST177 in HPS without protein) and plotted against $c_{protein}$ [µM]. Non-linear regression analysis was performed (using GraphPad PRISM 7, GraphPad Software Inc.) with a "one-site specific binding" saturation model to calculate the binding constant (equations are found in the SI).

3 Results and discussion

3.1 Photophysical characterization of 6-FAM-derivatives

As mentioned before, green-emitting fluorescein derivatives are among the most frequently used fluorophores for biological applications, such as in assays [26–28], fluorescence microscopy [29], and flow cytometry [30, 31], among others [32, 33]. The UV–vis absorption spectra of 6-FAM-SST177 and of the corresponding 6-FAM-azide in H_2O and in HPS buffer at different pH values are shown in

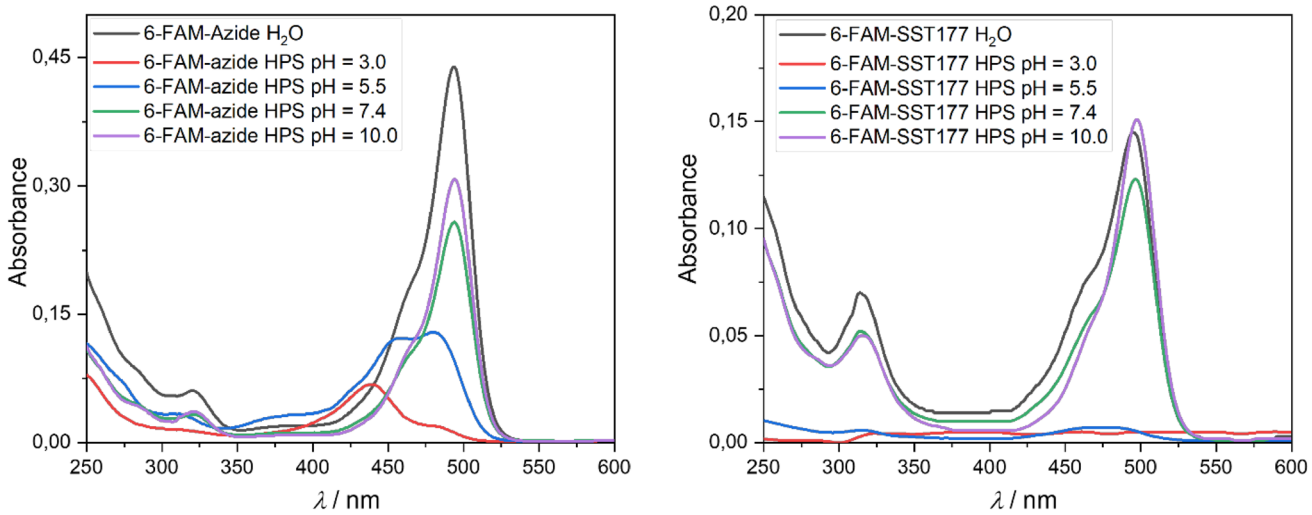

Fig. 1 Room-temperature absorption spectra of 6-FAM-azide (left) and S100A9-targeting 6-FAM-SST177 (right), measured in H_2O and HPS buffer at pH = 3.0, pH = 5.5, pH = 7.4 and pH = 10.0. In all cases, the concentration was kept constant ($c_{probe} \approx 10$ µM)

Fig. 1. The pH-dependency of the photophysical properties of fluorescein derivatives is well-reported in the literature and is attributed to cationic (pH = 3.0), neutral (pH = 5.5), monoanionic (pH = 7.4) and dianionic (pH > 12.0) species [34–37]. 6-FAM-azide shows the expected absorption maximum at λ_{max} = 495 nm in H_2O and neutral (pH = 7.4) to basic (pH = 10.0) buffers, which is attributed to the monoanionic species. Under acidic conditions (pH = 5.5 and pH = 3.0), the monoanion peak decreases, while the shoulder at λ = 465 nm (in neutral and basic) becomes dominant and gets blue-shifted to λ = 455 nm and 440 nm at pH = 5.5 and pH = 3.0, respectively. This reflects the acid–base equilibrium shifting from monoanionic to neutral and cationic species. Interestingly, as depicted in Fig. 1, the absorption spectra of 6-FAM in H_2O and a neutral or basic buffer are not significantly affected by conjugation to the targeting 2-amino benzimidazole-based lead structure in 6-FAM-SST177. On the other hand, under acidic conditions, no proper absorption spectra could be recorded. Apparently, conjugation prevents the formation of the luminescent cationic species in acidic conditions or reduces the overall absorption below the detection limit at the measured concentration. In addition, both Φ_F and τ_F were measured for all conditions (Table 1), where the effect of the conjugation of the dye to the 2-amino benzimidazole-based targeting structure can be evidenced. As shown herein, while for the non-conjugated 6-FAM-azide the obtained values are in the expected range both in H_2O and in neutral/basic buffer ($\Phi_F \approx 0.80$ and $\tau_F \approx 4$ ns), the conjugate 6-FAM-SST177 suffers from a dramatic drop in both Φ_F and τ_F under the same conditions (Table 1). As expected from the absorption spectra (Fig. 1), in more acidic conditions (pH = 3.0), no proper Φ_F could be reliably measured and τ_F was significantly shortened (Table 1). The effect of conjugation to the S100A9-targeting unit becomes clearer by comparing the radiative and non-radiative decay rate constants k_r and k_{nr} (Table 1, equations for calculations are

Table 1 Fluorescence quantum yields (Φ_F), fluorescence lifetimes (τ_F), radiative (k_r) and non-radiative decay (k_{nr}) constants of 6-FAM-azide and S100A9-targeting 6-FAM-SST177 in H_2O and HPS buffer at pH = 3.0, pH = 5.5, pH = 7.4 and pH = 10.0, as well as in the presence of murine S100A9

Sample	$\Phi_F \pm 0.02$	τ_F [ns]	k_r [10^5 s^{-1}]	k_{nr} [10^5 s^{-1}]
6-FAM-azide H_2O	0.77	$\tau = 4.13 \pm 0.01$	1.86 ± 0.05	0.56 ± 0.06
6-FAM-SST177 H_2O	0.07	$\tau_1 = 0.53 \pm 0.02$ (46%) $\tau_2 = 2.143 \pm 0.008$ (54%) $\tau_{av\_amp} = 1.39 \pm 0.03$	0.5 ± 0.2	6.69 ± 0.03
6-FAM-azide HPS pH = 7.4	0.69	$\tau = 3.93 \pm 0.01$	1.76 ± 0.06	0.79 ± 0.06
6-FAM-SST177 HPS pH = 7.4	0.07	$\tau_1 = 2.053 \pm 0.009$ (48%) $\tau_2 = 0.34 \pm 0.02$ (52%) $\tau_{av\_amp} = 1.16 \pm 0.06$	0.7 ± 0.2	9.49 ± 0.04
6-FAM-azide HPS pH = 3.0	0.27	$\tau = 2.80 \pm 0.01$	0.97 ± 0.07	2.62 ± 0.09
6-FAM-SST177 HPS pH = 3.0	n.d.	$\tau_1 = 2.51 \pm 0.04$ (17%) $\tau_2 = 1.22 \pm 0.08$ (11%) $\tau_3 = 0.080 \pm 0.007$ (72%) $\tau_{av\_amp} = 0.62 \pm 0.06$	n.d.	n.d.
6-FAM-azide HPS pH = 5.5	0.33	$\tau = 3.01 \pm 0.01$	1.10 ± 0.07	2.23 ± 0.08
6-FAM-SST177 HPS pH = 5.5	n.d.	$\tau_1 = 0.9 \pm 0.1$ (20%) $\tau_2 = 2.20 \pm 0.04$ (33%) $\tau_3 = 0.14 \pm 0.02$ (47%) $\tau_{av\_amp} = 0.99 \pm 0.07$	n.d.	n.d.
6-FAM-azide HPS pH = 10.0	0.80	$\tau = 3.975 \pm 0.006$	2.02 ± 0.06	0.50 ± 0.06
6-FAM-SST177 HPS pH = 10.0	0.13	$\tau_1 = 1.980 \pm 0.006$ (33%) $\tau_2 = 0.41 \pm 0.02$ (77%) $\tau_{av\_amp} = 0.93 \pm 0.05$	1.8 ± 0.4	11.9 ± 0.9
6-FAM-azide S100A9, HPS pH = 7.4	0.67	$\tau = 3.794 \pm 0.009$	1.77 ± 0.06	0.87 ± 0.06
6-FAM-SST177 S100A9, HPS pH = 7.4	0.24	$\tau_1 = 4.44 \pm 0.04$ (72%) $\tau_2 = 1.9 \pm 0.2$ (28%) $\tau_{av\_amp} = 3.74 \pm 0.06$	0.64 ± 0.06	2.0 ± 0.1

For multiexponential decays, the amplitude-weighted average lifetimes (τ_{av_amp}) are given along with the different decay components and the corresponding relative amplitudes as percentages. The raw data can be found in Figs. S28–S39

Average radiative and radiationless deactivation rate constants as well as their uncertainties were obtained as described in the SI

In case of multiexponential decays, k_r and k_{nr} were calculated using the τ_{av_amp} [38]. n.d. = not detected

shown in the SI) of dye and dye-conjugate in H_2O and HPS pH = 7.4. While k_r is reduced by approximately factor 3, the k_{nr} is roughly tenfold increased. This suggests pronounced non-radiative deactivation pathways opened up by conjugation and intramolecular interaction of the fluorophore with the heteroaromatic benzimidazole moiety mediated by the 2-amino pyridine spacer.

In order to further evaluate the potential for fluorescence binding assays with S100A9, 1 µM solutions of dye-azide and conjugate in HPS buffer pH = 7.4 were measured in the presence of 3.5 µM murine S100A9. At this protein concentration, > 99% binding of targeted 6-FAM-SST177 can be assumed ($c_{protein} > 10$ $K_D = 324$ nM (95 nM SEM, average over n = 3), see assay section below). As observed in Fig. 1 and Fig. S23, neither binding towards murine S100A9 by 6-FAM-SST177, nor protein availability in the solution in case of the free dye-azide did have a substantial effect on the absorption spectra. Both resembled their corresponding spectra in HPS pH = 7.4 without protein. However, protein binding of 6-FAM-SST177 led to a threefold increase in the quantum yield, from $\Phi_F = 0.08$ (without protein) to 0.24 (with murine S100A9, see Table 1). Furthermore, its amplitude-weighted average fluorescence lifetime elongated from $\tau_{av\_amp} = 0.98$ ns to 3.72 ns upon protein binding, which is in the range of the unconjugated dye-azide reaching $\tau = 3.93$ ns in HPS pH = 7.4. This results in a radiative decay constant comparable to 6-FAM-SST177 in HPS pH = 7.4 without protein. In contrast, the non-radiative decay constant k_{nr} is lowered by approximately factor 5 in the presence of the protein, which can be explained by less interaction of fluorophore and targeting moiety upon binding. Interestingly, the presence of protein in solution did not have a significant effect on the photophysical properties of 6-FAM-azide, if compared with HPS pH = 7.4. In addition, the photoluminescence spectra of both 6-FAM-azide and its conjugate 6-FAM-SST177 were recorded in all previously described conditions (Fig. S21 and S22). With an emission maximum at $\lambda_{max} = 520$ nm in all probes and a shoulder peaking at $\lambda = 550$ nm, which is more pronounced in acidic conditions [34], the conjugation does not have a significant effect on the emission spectrum of 6-FAM-SST177 compared to the dye-azide precursor. Moreover, the presence of murine S100A9 did not have a significant influence (Fig. S23).

3.2 Photophysical characterization of BODIPY-derivatives

Orange-emitting BODIPY-TMR and red-emitting BODIPY-TR were chosen not only for their excellent Φ_F reaching up to 90%, but also for their relatively long excited state lifetimes (≈ 5 ns), which is optimal in fluorescence polarization/anisotropy assays [39–42]. The UV–vis absorption spectra of BODIPY-TMR-SST175, BODIPY-TR-SST176 and their corresponding dye-azides were recorded in DCM (Fig. 2). Due to the poor solubility of both the dye-azides and the conjugates in aqueous media [39], the samples were dissolved in a small amount of EtOH and diluted with the buffer to HPS/EtOH 5% for the characterization in HPS buffer (pH = 7.4, Fig. 2). In DCM, the absorption spectra of the four BODIPY-derivatives are characterized by one single band with $\lambda_{max} = 548$ nm and 594 nm for BODIPY-TMR and BODIPY-TR, respectively, as reported in the literature. In HPS buffer, the λ_{max} of BODIPY-TMR-azide is slightly blue-shifted to 438 nm, while the absorption peak of the conjugate BODIPY-TMR-SST175 is broadened but without a significant change at $\lambda_{max} = 548$ nm. A peak broadening

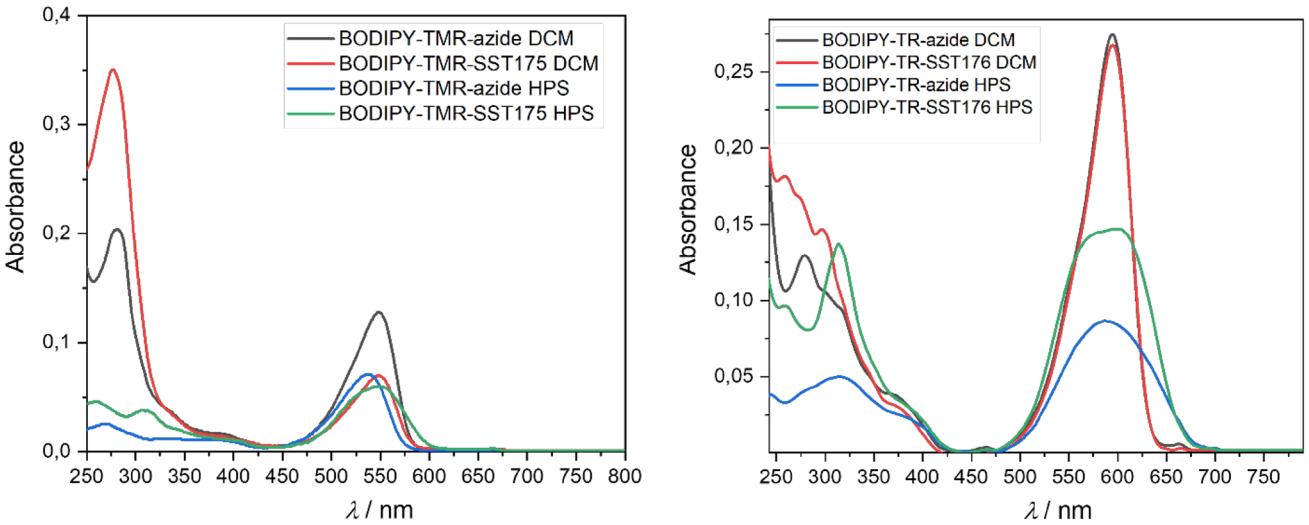

Fig. 2 Room-temperature absorption spectra of BODIPY-TMR- (left) and BODIPY-TR-derivatives in DCM and HPS buffer at pH = 7.4. In all cases, the concentration was kept constant ($c_{probe} \approx 10$ µM)

was also observed for both BODIPY-TR-derivatives in HPS buffer.

In addition, the photoluminescence spectra of BODIPY-TMR-azide with a $\lambda_{max} = 574$ nm was not significantly altered, neither upon conjugation to the 2-amino benzimidazole-based targeting unit nor in organic or aqueous solution (Fig. S24). This holds true for the emission spectrum of BODIPY-TR-azide with $\lambda_{max} = 623$ nm in HPS, but not for its conjugate BODIPY-TR-SST176 in the same buffer, where an aggregation-induced shoulder peaking on the red flank at $\lambda = 660$ nm appears (Fig. S25). Interestingly, a visible color-shift of BODIPY-TR-SST176 from bright pink (DCM) to fade blue (HPS/EtOH 5% pH = 7.4) was also observed by eye and upon illumination with a laser ($\lambda_{ex} = 405$ nm, Fig. 27). Fluorescence quantum yields and fluorescence lifetimes of the BODIPY-derivatives were measured in DCM and HPS/EtOH 5% (pH = 7.4) as well (Table 2). In DCM, the obtained quantum yields are $\Phi_F = 0.90$, 0.88, 0.92 and 0.72 for BODIPY-TMR-azide, BODIPY-TMR-SST175, BODIPY-TR-azide and BODIPY-TMR -SST176, respectively. These values are in concordance with the bibliography, but with a slight reduction upon conjugation for BODIPY-TR-SST176. This is most likely due to interaction of the heteroaromatic targeting structure with the thiazole moiety of BODIPY-TR, since it does not occur with the structurally similar BODIPY-TMR bearing a *p*-methoxyphenyl unit. Fluorescence lifetimes of both BODIPY-dyes of around 5 ns were obtained, in agreement with the bibliography for the four BODIPY-derivatives. In aqueous medium, again the low solubility and quenching through aggregation plays a major role, especially for both conjugates. This is manifested in low fluorescence quantum yields $\Phi_F = 0.05$, 0.07 and 0.02 for BODIPY-TMR-SST175, BODIPY-TR-azide and—BODIPY-TMR-SST176, respectively).

The quantum yield of the unconjugated BODIPY-TMR-azide is only slightly reduced to $\Phi_F = 0.71$ in buffer compared to 0.90 in DCM. In addition, a shortening of the fluorescence lifetimes was observed for both conjugates BODIPY-TMR–SST175 and BODIPY-TR-SST176 with $\tau_{av\_amp} = 2.92$ ns and 2.34 ns, respectively. On the other hand, the dye-azides kept their long lifetimes with a slight increase from 0.3 ns to 5.17 ns for BODIPY-TMR-azide and 5.60 ns for BODIPY-TR-azide, compared to the organic solvent. Because of the poor solubility and aggregation phenomena, we have refrained from measurements in the presence of murine S100A9.

3.3 Photophysical characterization of Cy5.5-derivatives

Cy5.5 was chosen as one of the most commonly used dyes for bioconjugates and small-molecule probes for NIR-based in vivo molecular imaging and various other applications [43–48]. Its high brightness, good photostability, excellent water-solubility and high contrast with respect to autofluorescence background originating from biological samples render it as an attractive label [46, 47]. The UV–vis absorption spectra of the targeted Cy5.5-SST110 conjugate and its Cy5.5-azide precursor were measured in H_2O, HPS (pH = 7.4) and in the presence of murine S100A9 (Fig. 3).

Table 2 Φ_F, τ_F, radiative (k_r) and non-radiative decay (k_{nr}) constants of BODIPY-TMR- and BODIPY-TR-derivatives in DCM and HPS buffer at pH = 7.4

Sample	$\Phi_F \pm 0.02$	τ_F [ns]	k_r [$10^5 s^{-1}$]	k_{nr} [$10^5 s^{-1}$]
BODIPY-TMR-azide DCM	0.90	$\tau = 4.856 \pm 0.009$	1.85 ± 0.04	0.21 ± 0.05
BODIPY-TMR-azide HPS	0.71	$\tau = 5.172 \pm 0.008$	1.37 ± 0.04	0.56 ± 0.05
BODIPY-TMR-SST175 DCM	0.88	$\tau = 4.81 \pm 0.02$	1.83 ± 0.05	0.25 ± 0.06
BODIPY-TMR-SST175 HPS	0.05	$\tau_1 = 2.0 \pm 0.1$ (45%) $\tau_2 = 3.6 \pm 0.1$ (55%) $\tau_{av\_amp} = 2.87 \pm 0.05$	0.17 ± 0.07	3.3 ± 0.2
BODIPY-TR-azide-DCM	0.92	$\tau = 5.60 \pm 0.01$	1.80 ± 0.04	0.16 ± 0.05
BODIPY-TR-azide HPS	0.07	$\tau = 5.11 \pm 0.01$	0.13 ± 0.03	1.66 ± 0.04
BODIPY-TR-SST176 DCM	0.72	$\tau_1 = 5.81 \pm 0.03$ (74%) $\tau_2 = 3.8 \pm 0.2$ (26%) $\tau_{av\_amp} = 5.30 \pm 0.03$	1.36 ± 0.04	0.53 ± 0.06
BODIPY-TR-SST176 HPS	0.02	$\tau_1 = 1.50 \pm 0.03$ (69%) $\tau_2 = 3.73 \pm 0.04$ (31%) $\tau_{av\_amp} = 2.18 \pm 0.02$	0.09 ± 0.09	4.2 ± 0.1

For multiexponential decays, the amplitude-weighted average lifetimes (τ_{av_amp}) are also given along with the different decay components and the corresponding relative amplitudes as percentages

The raw data can be found in Figs. S40–S47

Average radiative and radiationless deactivation rate constants as well as their uncertainties were obtained as described in the SI

In case of multiexponential decays, k_r and k_{nr} were calculated using the τ_{av_amp} [38]

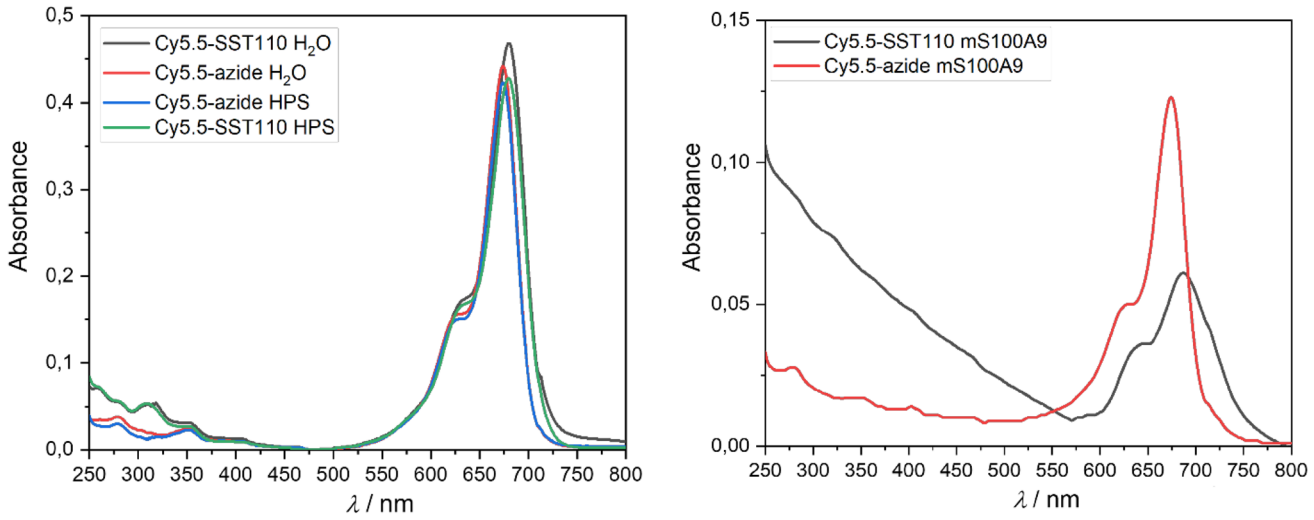

Fig. 3 Room-temperature absorption spectra of Cy5.5-azide and S100A9-targeting Cy5.5-SST110 (left) in water and HPS buffer at pH = 7.4 ($c_{probe} \approx 10$ µM), as well as in the presence of murine S100A9 (right, $c_{probe} = 1$ µM, $c_{protein} = 3.5$ µM)

In agreement with the literature, the reported Cy5.5 absorption peaks with a $\lambda_{max} = 674$ nm and a shoulder on the blue flank at $\lambda = 628$ nm for the azide in both H_2O and HPS were observed. Interestingly, a slightly red-shifted maximum with $\lambda_{max} = 680$ nm and $\lambda = 632$ nm shoulder was measured for the Cy5.5-SST110 conjugate. As depicted in Fig. 3, the presence of murine S100A9 did not affect the absorption spectrum of Cy5.5-azide, whereas the absorption spectrum of the targeted Cy5.5-SST110 appeared red-shifted and broadened to $\lambda_{max} = 688$ nm and $\lambda = 642$ nm for the blue flank shoulder. Additionally, a weak red-flank shoulder peaking at $\lambda = 715$ nm appeared. The photoluminescence spectra were recorded in H_2O, HPS (pH = 7.4) and in the presence of murine S100A9 as well (Fig. S26); in all cases, the emission spectra agreed with the literature ($\lambda_{max} = 702$ nm) [49]. However, conjugation to the targeting structure led to a 10 nm bathochromic shift to $\lambda_{max} = 712$ nm for Cy5.5-SST110 in both conditions. In addition, the presence of protein shifted the emission maxima of both probes into the red to $\lambda_{max} = 691$ nm and 695 nm, for Cy5.5-azide and Cy5.5-SST110, respectively. Since this shift appears in both the non-targeted and the conjugated probe, we assign these shifts to a solvent effect, probably resulting from the change in chemical surrounding of the protein solution compared to pure HPS buffer.

The recorded quantum yields ($\Phi_F = 0.22$) were in excellent agreement with the literature for both Cy5.5-derivatives in aqueous solutions, without the presence of protein (Table 3) [49]. No aggregation or quenching phenomena were observed. Most likely, the highly charged dye is able to compensate for solubility issues of the nonpolar, 2-amino benzimidazole-based targeting structure in Cy5.5-SST110. As shown in Table 3, the quantum yields are affected by the presence of murine S100A9. Proximity of the conjugate Cy5.5-SST110 to the protein upon binding leads to a quenching from $\Phi_F = 0.22$ to $\Phi_F = 0.05$. On the other hand, the quantum yield of Cy5.5-azide is slightly increased in the presence of the protein, which might be attributed to micro-environmental effects upon unspecific binding.

The fluorescence lifetimes appear slightly elongated from 0.94 ns and 0.95 ns to 1.22 ns and 1.22 ns for the Cy5.5-SST110 conjugate in H_2O and HPS (pH = 7.4), respectively, compared to the dye-azide precursor. The presence of the protein slightly shortens the lifetime of Cy5.5-azide, which again is attributed to unspecific binding effects. However, no substantial change in lifetime upon binding of Cy5.5-SST110 was observed, compared to the unbound probe. In summary, conjugation to the S100A9-targeting 2-amino benzimidazole-based lead structure in Cy5.5-SST110 did not significantly affect the photophysical properties of Cy5.5 in aqueous solution and physiological buffer, as seen from the comparison of the conjugate with the dye-azide precursor. However, the drop of Φ_F in the presence of murine S100A9 deterred us from further protein interaction studies and is also a constrain for potential NIR imaging studies.

3.4 Determination of K_D of 6-FAM-SST177 at mS100A9

The dissociation equilibrium constant K_D of 6-FAM-SST177 from murine S100A9 was determined in fluorometric measurements on a multi-well plate reader. As it was mentioned in the previous section, the fluorescence of 6-FAM-SST177 is dramatically quenched to $\Phi_F = 0.07$ in HPS buffer (pH = 7.4). Surprisingly, upon binding to the murine S100A9, the quantum yield rises to $\Phi_F = 0.24$, which

Table 3 Φ_F, τ_F, radiative (k_r) and non-radiative decay (k_{nr}) constants of Cy5.5-azide and S100A9-targeting Cy5.5-SST110 in H_2O and HPS buffer at pH = 7.4, as well as in the presence of murine S100A9

Sample	$\Phi_F \pm 0.02$	τ_F [ns]	k_r [$10^5 s^{-1}$]	k_{nr} [$10^5 s^{-1}$]
Cy5.5-Azide H_2O	0.22	$\tau = 0.937 \pm 0.002$	2.3 ± 0.2	8.3 ± 0.4
Cy5.5-Azide HPS pH = 7.4	0.22	$\tau = 0.947 \pm 0.005$	2.3 ± 0.2	8.2 ± 0.4
Cy5.5-SST110 H_2O	0.21	$\tau = 1.217 \pm 0.005$	1.7 ± 0.2	6.5 ± 0.3
Cy5.5-SST110 pH = 7.4	0.22	$\tau = 1.22 \pm 0.02$	1.8 ± 0.2	6.4 ± 0.3
Cy5.5-azide with mS100A9 in HPS pH = 7.4	0.29	$\tau = 0.897 \pm 0.006$	3.3 ± 0.04	8.1 ± 0.9
Cy5.5-SST110 with mS100A9 in HPS pH = 7.4	0.05	$\tau_1 = 1.77 \pm 0.06$ (49%) $\tau_2 = 0.80 \pm 0.08$ (51%) $\tau_{av\_amp} = 1.27 \pm 0.04$	0.4 ± 0.2	7.5 ± 0.4

For multiexponential decays, the amplitude-weighted average lifetimes (τ_{av_amp}) are given along with the different decay components and the corresponding relative amplitudes as percentages

The raw data can be observed in Fig. S48–S53

Average radiative and radiationless deactivation rate constants as well as their uncertainties were obtained as described in the SI

In case of multiexponential decays, k_r and k_{nr} were calculated using the τ_{av_amp} [38]

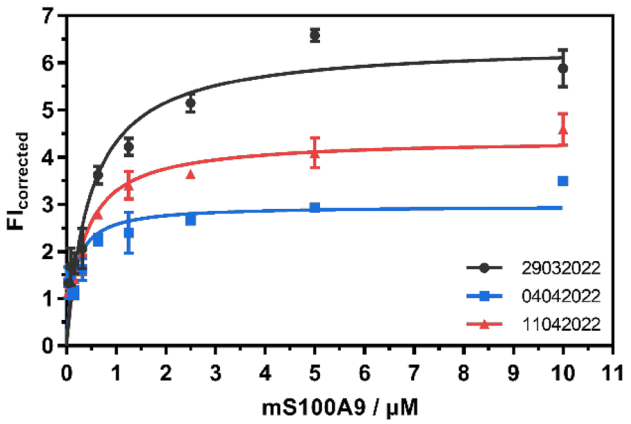

Fig. 4 Plot of protein background-corrected and blank-normalized fluorescence intensity of 6-FAM-SST177 versus concentration of murine S100A9, resulting in a saturation binding curve. The independent experiments were repeated on three different days (black, red, blue; the numbers indicate the corresponding dates). The dissociation equilibrium constant K_D was calculated as 324 nM (95 nM SEM average over $n = 3$) applying non-linear regression in a "one-site—specific binding" model

corresponds to an approximately three-fold increase. This boost in fluorescence intensity upon binding of 6-FAM-SST177 provides the read-out signal for the K_D determination. Samples with a fixed concentration of 6-FAM-SST177 (25 nM) and increasing concentrations of murine S100A9 from 40 nM to 10 µM in HPS (pH = 7.4) were prepared as duplicates. The measurements were performed on three independent experiments. Fluorescence intensities were measured and plotted as protein-background-corrected and blank-normalized intensities against the concentration of murine S100A9. This resulted in the saturation binding-curves shown in Fig. 4. The approximately three to five-fold fluorescence intensity increase from blank (25 nM 6-FAM-SST177 in HPS without protein) to binding saturation conditions at 10 µM murine S100A9 is in line with the rise of Φ_F. From these curves, the dissociation equilibrium constant was calculated as $K_D = 324$ nm (95 nM SEM average over n = 3, equations in S5), applying a non-linear regression in a "one-site specific binding model" (equations shown in the SI). As negative control experiments, non-binding 6-FAM-azide *vs*. murine S100A9 as well as 6-FAM-SST177 *vs*. murine S100A8 (Fig. S57) were evaluated under the same conditions. In both cases, no effects of increasing protein concentration on the fluorescence intensity were observed.

In summary, the determined K_D of approximately 300 nM confirms that the underlying 2-amino benzimidazole-based lead structure is eligible for in vitro S100A9 binding assays. Furthermore, Slatter *et al.* reported the development of a fluorescence intensity assay for the mitotic serine/threonine protein kinase Aurora-A using an Aurora-A-binding 6-FAM-derivative, applying a quenching phenomenon analog to our findings [50]. This additionally supports the use of 6-FAM-SST177 in future in vitro binding assays.

4 Conclusion

In our study, we demonstrated that a full photophysical characterization of fluorescent dye conjugates is crucial to assess the suitability of dye labels, and we found that only one particular S100A9-targeting conjugate turned out to be eligible for biological applications without any constrains (despite using four excellent and well-established organic fluorophores, namely 6-FAM, BODIPY-TMR, BODIPY-TR and Cy5.5). The fluorescein derivative 6-FAM-SST177 showed quenching in aqueous media upon

conjugation with the targeting unit, which resulted in a low quantum yield and fast non-radiative decay compared to its azide precursor. Presumably, the interaction between the fluorophore and the targeting moiety open up non-radiative pathways, which are less pronounced upon binding to murine S100A9. Hence, the determination of its protein-dissociation equilibrium constant in the 300 nM range was possible and the increased fluorescence intensities upon binding to murine S100A9. This serves as an outlook for future applications of 6-FAM-SST177 for in vitro assays. In contrast, the conjugate Cy5.5-SST110 showed excellent photophysical properties in H_2O and in buffers, but its fourfold drop of Φ_F in the presence of protein represents a major constraint towards in vitro and in vivo applications. Furthermore, both BODIPY-conjugates, which were initially considered for fluorescence polarization/anisotropy assays due to their relatively long fluorescence lifetimes, suffered from significant quenching and aggregation phenomena in aqueous media. This is attributed to their poor solubility and they had to be excluded from in vitro nor in vivo studies as well. In general, it appears abundantly clear that solubility, aggregation and quenching phenomena (before and after conjugation with a targeting moiety as well as upon binding to a biological target) need to be seriously assessed and considered while developing a fluorescent bioimaging agent. In conclusion, in the present study we have overcome the intrinsic limitations towards a binding assay involving an inflammation marker.

Supplementary Information The online version contains supplementary material available at https://doi.org/10.1007/s43630-023-00432-2.

Acknowledgements This project has received funding from the Innovative Medicines Initiative 2 Joint Undertaking (JU) under grant agreement No 831514 (Immune-Image). The JU receives support from the European Union's Horizon 2020 research and innovation program and EFPIA. S.T.S. was supported by CiM-IMPRS Graduate School, Münster as a member. We gratefully thank *Prof. Thomas Vogl*, Institute for Immunology, University Hospital Münster, Germany, for providing murine S100A9 for interaction studies. C.A.S., A.F. and G.F. gratefully acknowledge financial support from the DFG–Collaborative Research Centre (CRC) 1450–431460824, Münster, Germany (projects A02 and A03). C.A.S. would like to acknowledge the DFG (EXC 1003 Cluster of Excellence Cells in Motion) as well as DFG/Land NRW (INST 211/915-1 FUGG: "Integrated confocal luminescence spectrometer with spatiotemporal resolution and multiphoton excitation") for generous financial support.

Authors contribution The manuscript was written with the contributions of all authors. All authors have given approval for the final version of the manuscript.

Funding Open Access funding enabled and organized by Projekt DEAL.

Data availability Not applicable.

Declarations

Conflict of interest The authors declare no financial or non-financial conflicts of interest.

References

1. Foell, D., Wittkowski, H., Vogl, T., & Roth, J. (2007). S100 proteins expressed in phagocytes: a novel group of damage-associated molecular pattern molecules. *Journal of Leukocyte Biology, 81*, 28–37. https://doi.org/10.1189/jlb.0306170
2. Foell, D., & Roth, J. (2004). Proinflammatory S100 proteins in arthritis and autoimmune disease. *Arthritis and Rheumatism, 50*, 3762–3771. https://doi.org/10.1002/art.20631
3. Chang, K.-A., Kim, H. J., & Suh, Y.-H. (2012). The role of S100a9 in the Pathogenesis of Alzheimer's Disease: the therapeutic effects of S100a9 knockdown or knockout. *Neuro-Degenerative Diseases, 10*, 27–29. https://doi.org/10.1159/000333781
4. Arai, K., Takano, S., Teratani, T., Ito, Y., Yamada, T., & Nozawa, R. (2008). S100A8 and S100A9 overexpression is associated with poor pathological parameters in invasive ductal carcinoma of the breast. *Current Cancer Drug Targets, 8*, 243–252. https://doi.org/10.2174/156800908784533445
5. Björk, P., Björk, A., Vogl, T., Stenström, M., Liberg, D., Olsson, A., Roth, J., Ivars, F., & Leanderson, T. (2009). Identification of human S100A9 as a novel target for treatment of autoimmune disease via binding to quinoline-3-carboxamides. *PLoS Biology, 7*, 0800–0812. https://doi.org/10.1371/journal.pbio.1000097
6. Averill, M. M., Kerkhoff, C., & Bornfeldt, K. E. (2012). S100A8 and S100A9 in cardiovascular biology and disease. *Arteriosclerosis, Thrombosis, and Vascular Biology, 32*, 223–229. https://doi.org/10.1161/ATVBAHA.111.236927
7. Reilmann, R., Gordon, M. F., Anderson, K. E., Feigin, A., Tabrizi, S. J., Leavitt, B. R., Stout, J. C., Piccini, P., Rynkowski, G., Volkinshtein, R., Savola, J. (2018). J05 Legato-hd study: a phase 2 study assessing the efficacy and safety of laquinimod as a treatment for huntington disease. *Clinical Therapeutics*, BMJ Publishing Group Ltd, p. A99.2-A99. https://doi.org/10.1136/jnnp-2018-EHDN. 265.
8. D'Haens, G., Sandborn, W. J., Colombel, J. F., Rutgeerts, P., Brown, K., Barkay, H., Sakov, A., Haviv, A., & Feagan, B. G. (2015). A phase II study of laquinimod in Crohn's disease. *Gut, 64*, 1227–1235. https://doi.org/10.1136/gutjnl-2014-307118
9. Escudier, B., Faivre, S., van Cutsem, E., Germann, N., Pouget, J.-C., Plummer, R., Vergote, I., Thistlethwaite, F., Bjarnason, G. A., Jones, R., Mackay, H., Edeline, J., Fartoux, L., Hirte, H., & Oza, A. (2017). A phase II multicentre, open-label, proof-of-concept study of tasquinimod in hepatocellular, ovarian, renal cell, and gastric cancers, *Target*. *Oncologia, 12*, 655–661. https://doi.org/10.1007/s11523-017-0525-2

10. Pili, R., Häggman, M., Stadler, W. M., Gingrich, J. R., Assikis, V. J., Björk, A., Nordle, Ö., Forsberg, G., Carducci, M. A., & Armstrong, A. J. (2011). Phase II randomized, double-blind, placebo-controlled study of tasquinimod in men with minimally symptomatic metastatic castrate-resistant prostate cancer. *J. Clin. Onco., 29*, 4022–4028. https://doi.org/10.1200/JCO.2011.35.6295.
11. Vollmer, T. L., Sorensen, P. S., Selmaj, K., Zipp, F., Havrdova, E., Cohen, J. A., Sasson, N., Gilgun-Sherki, Y., & Arnold, D. L. (2014). A randomized placebo-controlled phase III trial of oral laquinimod for multiple sclerosis. *Journal of Neurology, 261*, 773–783. https://doi.org/10.1007/s00415-014-7264-4
12. Vogl, T., Eisenblätter, M., Völler, T., Zenker, S., Hermann, S., van Lent, P., Faust, A., Geyer, C., Petersen, B., Roebrock, K., Schäfers, M., Bremer, C., & Roth, J. (2014). Alarmin S100A8/S100A9 as a biomarker for molecular imaging of local inflammatory activity. *Nature Communications, 5*, 4593. https://doi.org/10.1038/ncomms5593
13. Faust, A., Völler, T., Busch, F., Schäfers, M., Roth, J., Hermann, S., & Vogl, T. (2015). Development and evaluation of a non-peptidic ligand for the molecular imaging of inflammatory processes using S100A9 (MRP14) as a novel target. *Chemical Communications, 51*, 15637–15640. https://doi.org/10.1039/c5cc07019h
14. Völler, T., Faust, A., Roth, J., Schäfers, M., Vogl, T., & Hermann, S. (2018). A Non-Peptidic S100A9 specific ligand for optical imaging of phagocyte activity In Vivo. *Molecular Imaging and Biology, 20*, 407–416. https://doi.org/10.1007/s11307-017-1148-9.
15. Lakowicz, J. R. (2006). *Principles of Fluorescence Spectroscopy*. Springer. https://doi.org/10.1007/978-0-387-46312-4.
16. Zhang, X., Bloch, S., Akers, W., Achilefu, S. (2012). Near-Infrared Molecular Probes for In Vivo Imaging. *Current Protocols in Cytometry*, John Wiley & Sons, Inc., Hoboken, NJ, USA. https://doi.org/10.1002/0471142956.cy1227s60.
17. Bucevičius, J., Kostiuk, G., Gerasimaitė, R., Gilat, T., & Lukinavičius, G. (2020). Enhancing the biocompatibility of rhodamine fluorescent probes by a neighbouring group effect. *Chemical Science, 11*, 7313–7323. https://doi.org/10.1039/D0SC02154G
18. Alamudi, S. H., & Chang, Y.-T. (2018). Advances in the design of cell-permeable fluorescent probes for applications in live cell imaging. *Chemical Communications, 54*, 13641–13653. https://doi.org/10.1039/C8CC08107G
19. Grimm, J. B., English, B. P., Chen, J., Slaughter, J. P., Zhang, Z., Revyakin, A., Patel, R., Macklin, J. J., Normanno, D., Singer, R. H., Lionnet, T., & Lavis, L. D. (2015). A general method to improve fluorophores for live-cell and single-molecule microscopy. *Nature Methods, 12*, 244–250. https://doi.org/10.1038/nmeth.3256
20. Oliveira, E., Bértolo, E., Núñez, C., Pilla, V., Santos, H. M., Fernández-Lodeiro, J., Fernández-Lodeiro, A., Djafari, J., Capelo, J. L., & Lodeiro, C. (2018). Green and red fluorescent dyes for translational applications in imaging and sensing analytes: a dual-color flag. *ChemistryOpen, 7*, 9–52. https://doi.org/10.1002/open.201700135
21. M. Bainbridge, S. East, M. Ekblad, J. Hargrave, D. Liberg, N. Prevost, U. Welmar, Novel compounds useful as S100-inhibitors, WO2015177367A1, 2015.
22. Jansson, K., Fristedt, T., Olsson, A., Svensson, B., & Jönsson, S. (2006). Synthesis and reactivity of laquinimod, a Quinoline-3-carboxamide: intramolecular transfer of the enol proton to a nitrogen atom as a plausible mechanism for ketene formation. *Journal of Organic Chemistry, 71*, 1658–1667. https://doi.org/10.1021/jo052368q
23. Adamczyk, M., Fishpaugh, J. R., & Heuser, K. J. (1997). Preparation of succinimidyl and pentafluorophenyl active esters of 5- and 6- carboxyfluorescein. *Bioconjugate Chemistry, 8*, 253–255. https://doi.org/10.1021/bc9600877
24. Aksinenko, A. Y., Pushin, A. N., & Sokolov, V. B. (2002). A convenient synthesis of 3,3,3-trifluoroalanine derivatives. *Russ. Chem. Bull. Int. Ed., 51*, 2136–2138. https://doi.org/10.1023/A:1021692717142.
25. Sucunza, D., Samadi, A., Chioua, M., Silva, D. B., Yunta, C., Infantes, L., Carmo Carreiras, M., Soriano, E., & Marco-Contelles, J. (2011). A practical two-step synthesis of imidazo[1,2-a]pyridines from N-(prop-2-yn-1-yl)pyridin-2-amines. *Chemical Communications, 47*, 5043. https://doi.org/10.1039/c1cc10641d
26. Kobatake, E., Sasakura, H., Haruyama, T., Laukkanen, M. L., Keinänen, K., & Aizawa, M. (1997). A fluoroimmunoassay based on immunoliposomes containing genetically engineered lipid-tagged antibody. *Analytical Chemistry, 69*, 1295–1298. https://doi.org/10.1021/ac961162+
27. Pinals, R. L., Yang, D., Lui, A., Cao, W., & Landry, M. P. (2020). Corona exchange dynamics on carbon nanotubes by multiplexed fluorescence monitoring. *Journal of the American Chemical Society, 142*, 1254–1264. https://doi.org/10.1021/jacs.9b09617
28. Turek-Etienne, T. C., Small, E. C., Soh, S. C., Xin, T. A., Gaitonde, P. V., Barrabee, E. B., Hart, R. F., & Bryant, R. W. (2003). Evaluation of fluorescent compound interference in 4 fluorescence polarization assays: 2 kinases, 1 protease, and 1 phosphatase. *SLAS Discovery, 8*, 176–184. https://doi.org/10.1177/1087057103252304
29. R. W., Horobin, J. A. Kiernan, *Conn's Biological Stains*, Taylor & Francis, 2020. https://doi.org/10.1201/9781003076841.
30. Illien, F., Rodriguez, N., Amoura, M., Joliot, A., Pallerla, M., Cribier, S., Burlina, F., & Sagan, S. (2016). Quantitative fluorescence spectroscopy and flow cytometry analyses of cell-penetrating peptides internalization pathways: optimization, pitfalls, comparison with mass spectrometry quantification. *Science and Reports, 6*, 36938. https://doi.org/10.1038/srep36938
31. Slight, R. D., Ferguson, R., Stirling, D., Mcclelland, D. B. L., & Mankad, P. S. (2009). Experience with sodium fluorescein flow cytometry in the determination of red cell volume. *International Journal of Laboratory Hematology, 31*, 233–235. https://doi.org/10.1111/j.1751-553X.2008.01029.x
32. Lee, R., Erstling, J. A., Hinckley, J. A., Chapman, D. V., & Wiesner, U. B. (2021). addressing particle compositional heterogeneities in super-resolution-enhanced live-cell ratiometric pH sensing with ultrasmall fluorescent core-shell aluminosilicate nanoparticles. *Advanced Functional Materials, 31*, 2106144. https://doi.org/10.1002/adfm.202106144
33. Bradley, M., Alexander, L., Duncan, K., Chennaoui, M., Jones, A. C., & Sánchez-Martín, R. M. (2008). pH sensing in living cells using fluorescent microspheres. *Bioorganic & Medicinal Chemistry Letters, 18*, 313–317. https://doi.org/10.1016/j.bmcl.2007.10.075
34. Martin, M. M., & Lindqvist, L. (1975). The pH dependence of fluorescein fluorescence. *Journal of Luminescence, 10*, 381–390. https://doi.org/10.1016/0022-2313(75)90003-4
35. Doughty, M. J. (2010). pH dependent spectral properties of sodium fluorescein ophthalmic solutions revisited. *Ophthalmic and Physiological Optics, 30*, 167–174. https://doi.org/10.1111/j.1475-1313.2009.00703.x
36. Slyusareva, E. A., & Gerasimova, M. A. (2014). pH-dependence of the absorption and fluorescent properties of fluorone dyes in aqueous solutions. *Russian Physics Journal, 56*, 1370–1377. https://doi.org/10.1007/s11182-014-0188-8
37. Zanker, V., & Peter, W. (1958). Die prototropen formen des fluoresceins. *Chemische Berichte, 91*, 572–580. https://doi.org/10.1002/cber.19580910316

38. Sillen, A., & Engelborghs, Y. (1998). The correct use of 'average' fluorescence parameters. *Photochemistry and Photobiology, 67*, 475–486. https://doi.org/10.1111/j.1751-1097.1998.tb09082.x
39. Courtis, A. M., Santos, S. A., Guan, Y., Hendricks, J. A., Ghosh, B., Szantai-Kis, D. M., Reis, S. A., Shah, J. V., & Mazitschek, R. (2014). Monoalkoxy BODIPYs—a fluorophore class for bioimaging. *Bioconjugate Chemistry, 25*, 1043–1051. https://doi.org/10.1021/bc400575w
40. Koch, P. D., Quintana, J., Ahmed, M. S., Kohler, R. H., & Weissleder, R. (2021). Small molecule imaging agent for mutant KRAS G12C. *Advanced Therapeutics (Weinh), 4*, 2000290. https://doi.org/10.1002/adtp.202000290
41. Duckworth, B. P., & Aldrich, C. C. (2010). Development of a high-throughput fluorescence polarization assay for the discovery of phosphopantetheinyl transferase inhibitors. *Analytical Biochemistry, 403*, 13–19. https://doi.org/10.1016/j.ab.2010.04.009
42. Lea, W. A., & Simeonov, A. (2011). Fluorescence polarization assays in small molecule screening. *Expert Opinion on Drug Discovery, 6*, 17–32. https://doi.org/10.1517/17460441.2011.537322
43. Um, W., Park, J., Youn, A., Cho, H., Lim, S., Lee, J. W., Yoon, H. Y., Lim, D.-K., Park, J. H., & Kim, K. (2019). A comparative study on albumin-binding molecules for targeted tumor delivery through covalent and noncovalent approach. *Bioconjugate Chemistry, 30*, 3107–3118. https://doi.org/10.1021/acs.bioconjchem.9b00760
44. Zhang, Y., Wang, M., Liu, W., & Peng, X. (2019). Optical imaging of triple-negative breast cancer cells in xenograft athymic mice using an ICAM-1-targeting small-molecule probe. *Molecular Imaging and Biology, 21*, 835–841. https://doi.org/10.1007/s11307-018-01312-3
45. Weissleder, R., Kelly, K., Sun, E. Y., Shtatland, T., & Josephson, L. (2005). Cell-specific targeting of nanoparticles by multivalent attachment of small molecules. *Nature Biotechnology, 23*, 1418–1423. https://doi.org/10.1038/nbt1159
46. Chen, K., Yap, L.-P., Park, R., Hui, X., Wu, K., Fan, D., Chen, X., & Conti, P. S. (2012). A Cy5.5-labeled phage-displayed peptide probe for near-infrared fluorescence imaging of tumor vasculature in living mice. *Amino Acids, 42*, 1329–1337. https://doi.org/10.1007/s00726-010-0827-5
47. Ballou, B., Fisher, G. W., Deng, J. S., Hakala, T. R., Srivastava, M., & Farkas, D. L. (1998). Cyanine fluorochrome-labeled antibodies in vivo: assessment of tumor imaging using Cy3, Cy5, Cy5.5, and Cy7. *Cancer Detection Prevention, 22*, 251–257. https://doi.org/10.1046/j.1525-1500.1998.0oa25.x
48. Hahn, C. D., Riener, C. K., & Gruber, H. J. (2001). Labeling of Antibodies with Cy3-, Cy3.5-, Cy5-, and Cy5.5-monofunctional Dyes at Defined Dye/Protein Ratios. *Single Molecules, 2*, 149–149. https://doi.org/10.1002/1438-5171(200107)2:23.0.CO;2-5.
49. Klehs, K., Spahn, C., Endesfelder, U., Lee, S. F., Fürstenberg, A., & Heilemann, M. (2014). Increasing the brightness of cyanine fluorophores for single-molecule and superresolution imaging. *ChemPhysChem, 15*, 637–641. https://doi.org/10.1002/cphc.201300874
50. Slatter, A. F., Campbell, S., & Angell, R. M. (2013). Development of a fluorescence intensity assay for the mitotic serine/threonine protein kinase aurora-A. *Journal of Biomolecular Screening, 18*, 219–225. https://doi.org/10.1177/1087057112459888